

Mechanical Properties of Fillet Weld Joints by Underwater Wet Welding in Repairing Corrosion-Damaged Offshore Steel Structures

Xiao Chen*, Yasuo Kitane**, Yoshito Itoh***

* M. of Eng., Doctoral student, Dept. of Civil Eng., Nagoya University, Furo-cho, Chikusa-ku, Nagoya, 464-8603

** Ph.D., Assist. Prof., Dept. of Civil Eng., Nagoya University, Furo-cho, Chikusa-ku, Nagoya, 464-8603

*** Dr. of Eng., Professor, Dept. of Civil Eng., Nagoya University, Furo-cho, Chikusa-ku, Nagoya, 464-8603

This paper presents a series of experiments on fourteen different assemblies of fillet weld joints produced by both underwater and in-air welding. Mechanical properties of underwater fillet welds in terms of strength, ductility, and failure modes are investigated in this study. Weld profiles, hardness distributions, and metallographic features of underwater welds are also examined. The study indicates that underwater fillet weld joints have larger strength but smaller ductility when compared with their counterpart in-air ones. The increase in strength ranges from 6.9% to 41.0%, and the decrease in ductility is about 50% for most of weld assembly types. Underwater fillet weld joints on corroded SY295 steel exhibit inferior ductility due to underbead cracks. Based on the test results, the paper proposes a practical method to model underwater welds in finite element analysis.

Keywords: underwater wet welding, fillet weld, strength, ductility, repair

1. INTRODUCTION

Underwater wet welding has long been recognized as one of the most common techniques to build, and particularly repair offshore steel structures, such as marine platforms, pier piles, pipelines, etc. Due to its high efficiency in time and relatively low cost, underwater wet welding is gaining more popularity for recent energy explorations into the sea^{1,2)}. Not surprisingly, over the past decades, a number of studies have been done on underwater wet welds on their metallurgical features^{3,4)}, influence of quenching⁵⁾, development of new electrodes suitable for underwater wet welding⁶⁾, etc. Although some studies have examined mechanical properties of underwater welds, they mainly focused on properties of weld materials^{7,8,9)}. Few studies have been carried out stressing on design of underwater fillet welds as joints, which are crucial parts of the structures to be built or repaired. Fig.1 shows a typical work of repairing offshore steel pipe piles and steel sheet piles by welding cover steel plates over corrosion-damaged areas. The structural portions to be repaired are usually located at splash and tidal zones, where severe corrosion damages occur.

The present *Port Steel Structure Corrosion-Prevention and*

*Repair Manual*¹⁰⁾, based on tests on forty-six fillet welded specimens conducted in 1985, discounts strength of fillet welds made in underwater wet environment by specifying as 80% of that of in-air welds when designing weld joints to repair corrosion damaged offshore structures for any base steels. Hence, the allowable stress of underwater welds ranges from 62 MPa for SS400, SM400, and SMA400 base steels to 94 MPa for SM490Y, SM520, and SMA490 base steels. Similarly, in *U.S. Navy Underwater Cutting & Welding Manual*¹¹⁾, the strength of underwater welds, which ranges from 34 MPa for mild base steels to 62 MPa for high strength base steels, is defined as the electrode strength divided by a safety factor of 6.

There are many offshore steel structures older than 40 years old in Japan, and many of which may require a repair work in the near future. To achieve an efficient and effective repair design for welding cover plates in underwater wet environments over corrosion-damaged areas, a load bearing capacity of the repaired structure will have to be accurately evaluated in the design process. The final goal of this research is to identify mechanical behavior of underwater fillet welds to be considered in the repair design and to propose design recommendations for efficient repair work using underwater wet welding. As the first

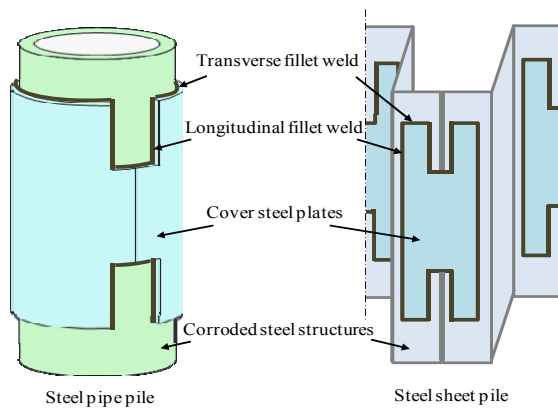


Fig.1 Repaired offshore steel structures using underwater welding

step towards the goal, this paper presents an experimental study on the strength and ductility of underwater fillet weld joints, and differences in mechanical properties between underwater welds and their counterpart in-air welds are investigated qualitatively as well as quantitatively. To better understand material features of underwater welds, Vickers hardness tests and microstructure examinations are also performed. Based on the obtained weld characteristics, the paper proposes a practical modeling method for those welds in finite element (FE) analysis.

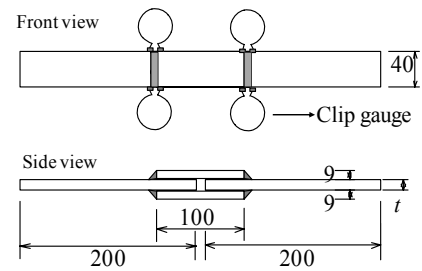
2. EXPERIMENTAL PROGRAM

Table 1 presents the test matrix indicating different weld assemblies with their designations and parameters. In total, fourteen types of different fillet weld assemblies are tested with respect to the two welding environments of in-air and underwater, the two weld orientations of transverse and longitudinal fillet welds, and the four base steels of SY295, SYW295, and corroded SY295 for steel sheet piles, and STK400 for steel pipes. SY295, SYW295, and STK400 are specified to have yield stresses of 295 MPa, 295 MPa, and 235 MPa in Japanese Industrial Standard (JIS) A5528, A5523, and G3444, respectively. Test results for STK400 were already presented in Ref. 12).

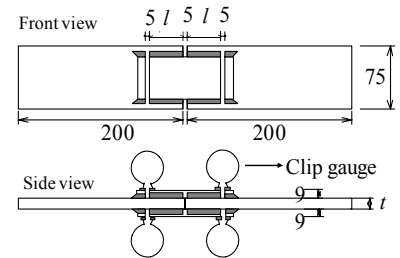
In this paper, the number following the weld designation is a specimen's number, and the number following the mark “#” is a weld bead number in the specimen. For example, LYA1#2 means No. 2 weld bead on the first specimen of LYA assembly type.

2.1 Test Specimens and Material Properties

Two configurations of specimens with different weld orientations according to JIS Z3131 and Z3132 are used for sheet pile specimens as well as pipe specimens as illustrated in Fig.2. The weld leg length is specified as 6 mm, a typical size used in repair welding in Japan. Two welders, with working experience of 24 years and 27 years, are assigned to in-air and



(a) Transverse specimen



$t=13$ or $6-8$ for sheet base $t=12.7$ for pipe base
 $l=40$ for pristine base $l=20$ for corroded base

(b) Longitudinal specimen

Fig.2 Specimen configuration (unit in mm)*

*Curvature of pipe is not depicted.

underwater welding work, respectively. One weld pass is used in welding process as used in real repair work, and the welding direction is specified in the same way for both underwater welds and in-air welds, that is from lower to upper for longitudinal welds and from left to right for transverse welds. Longitudinal welding is performed in the vertical position, while transverse welding is performed basically in the horizontal position which is close to the flat position for upper sides of transverse welds and the overhead position for lower sides of transverse welds. Welding of underwater specimens is performed in a 3-m deep seawater pool to simulate underwater welding performed on structural portions at the tidal zone. Also, welding conditions used in the study are specified to simulate those in real repair welding, and they are shown in Table 2.

Mechanical properties of steels, listed together with chemical compositions in Table 3, are obtained from static tensile coupon tests. To distinguish corroded and uncorroded SY295 steels, corroded SY295 base steel is referred to as CSY295 in this paper. It should be noted that CSY295 base plates with thickness varying from 6 to 8 mm were cut from in-situ steel sheet piles, which was exposed to marine environment for about 35 years at Kimitsu Works, Nippon Steel Corporation, Japan. CSY295 base plates are prepared to study corrosion effects, which are thickness reduction and surface roughness in this paper, on weld properties. Corrosion products on the base plates are removed completely by sand blasting. Table 4 lists thickness and surface roughness parameters of corroded SY295 steels. Surface roughness parameters are calculated based on surface profile data measured at Hiroshima

Table 1 Test matrix

Specimen designation	No. of specimens	Structural type	Welding environment	Weld orientation	Base steel	Base plate thickness(mm)	Weld length(mm)	Cover plate
TYA	3	Sheet pile	In-air	Transverse	SY295	13 mm	40 mm	SM490A (<i>t</i> =9 mm)
TWA	3				SYW295			
LYA	3			SY295				
LWA	3			Longitudinal	SYW295			
LCA	3				CSY295			
TYW	3		Transverse	SY295	13 mm	40 mm		
TWW	3			SYW294				
LYW	3		Underwater	SY295				
LWW	3			Longitudinal			SYW295	
LCW	2		CSY295	6-8 mm			20 mm	
TKA	4	Pipe (ϕ 216.3 mm)	In-air	Transverse	STK400	12.7 mm	40 mm	SM400B (<i>t</i> =9 mm)
LKA	4			Longitudinal				
TKW	4		Underwater	Transverse				
LKW	4			Longitudinal				

Table 2 Welding details

Case	Welding environment	Orientation	Current(A)	Voltage(V)	Welding velocity(mm/min)	Temperature (°C)	pH	Salinity (wt-%)
Sheet pile	In-air	Longitudinal	70-80	12-16	65-85	17	-	-
		Transverse	55-70	10-20	145-200			
	Underwater	Longitudinal	80-95	19-23	60-70	14	7.9	2.6
		Transverse	75-95	16-23	120-160			
Pipe*	In-air	Longitudinal	100-110	20-30	79	Not measured	-	-
		Transverse	90-100	20-40	88			
	Underwater	Longitudinal	120-140	20-40	79	25.6	8.2	2.1
		Transverse	120-140	20-40	88			

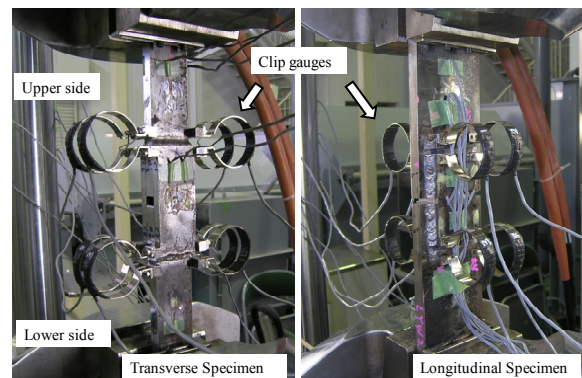
*Data for pipe are from Watanabe et al.¹²⁾

University. Prior to the weld strength tests, weld profiles are measured by a laser displacement sensor. Five equidistant cross sections along each weld bead are measured, and the weld leg length, size of throat, and weld size of each bead are calculated by averaging the five sections.

2.2 Test Setup

The specimens are tested under a quasi-static tensile loading using a 500 kN MTS material testing machine. Since there are two weld orientations, longitudinal welds are tested in shear while transverse welds are in tension. Deformation of individual weld is measured by clip gauges placed at the ends of each weld bead shown in Fig.2. Fig.3 illustrates the test setup. In this study, weld strength is defined as Eq. (1) according to JIS Z3131 and Z3132:

$$\sigma_w = \frac{P_{\max}}{n\bar{a}l} \quad (1)$$

**Fig.3** Test setup

where, σ_w is the average strength of fillet weld despite of nonuniform distribution of shear stress in longitudinal welds, P_{\max} is the maximum load, \bar{a} is the average throat size of all

Table 3 Material properties of steels

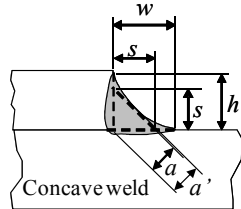
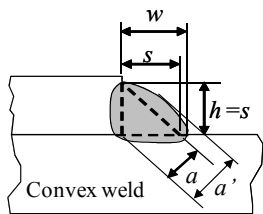
Material	Mechanical properties					Chemical compositions (wt-%)					
	Young's modulus, E(GPa)	Poisson's ratio, ν	Yield stress, σ_y (MPa)	Ultimate strength, σ_u (MPa)	Elongation, $\Delta\ell$ (%)	C	Si	Mn	P	S	CE _{ITW} *
SY295	213	0.29	273**	497	41	0.30	0.06	0.72	0.016	0.020	0.430
CSY295	212	0.29	349	531	34	0.27	0.02	0.96	0.013	0.019	0.433
SYW295	213	0.28	392	513	42	0.10	0.23	1.41	0.020	0.005	0.379
STK400	203	0.28	362	394	41	0.12	0.10	0.56	0.013	0.006	0.230
SM490A	209	0.28	361	532	39	0.16	0.34	1.44	0.015	0.007	0.457
SM400B	213	0.28	290	416	46	0.12	0.23	1.02	0.013	0.003	0.328
Electrode***	-	-	410	460	30	0.10	0.10	0.43	0.015	0.007	0.188

*CE_{ITW} = C+(Si+Mn)/6+(Cr+Mo+V)/5+(Ni+Cu)/15, only first two terms are used except SYW295. **Tested 273 MPa is smaller than specified 295 MPa. Verifications with steel manufacturer suggest that this is caused by variations in sampling regions on sheets coupled with differences between loading rates in coupon tests. ***Catalogue values provided by the manufacturer.

Table 4 Thickness and roughness parameters of patched area on corroded bases (unit in mm)

Patched area of specimen	Thickness parameter		Roughness parameter*					
	Average thickness	Standard deviation	Sea side			Soil side		
			Ra	Rz	Rq	Ra	Rz	Rq
LCA1	5.37	0.66	0.23	1.98	0.29	0.11	0.69	0.13
LCA2	6.69	0.69	0.23	1.85	0.30	0.19	1.11	0.22
LCA3	7.22	0.51	0.19	1.43	0.24	0.14	0.87	0.16
LCW1**	6.28	0.66	0.14	1.04	0.17	0.08	0.52	0.09
LCW2	6.51	0.57	0.19	1.41	0.23	0.06	0.50	0.07
LCW3	7.51	0.82	0.33	2.01	0.40	0.07	0.64	0.09

*Notation for roughness parameters is specified in JIS B 0601: 2001. Ra: Arithmetic mean height of the rough surface, Rz: Maximum height of the rough surface, Rq: Root mean square height of the rough surface. **LCW1 specimen is not used in the test due to misproduction.



w, h = weld leg length,
s = weld size, a = weld throat
a' = actual weld throat

Fig.4 Definition of weld size

welds in each specimen, l is the average weld length, and n is the number of welds in one cross section of the specimen, which is

Table 5 h/w values of welds

Welding environment	Structural type	Transverse		Longitudinal
		Upper	Lower	
In-air	Sheet pile	1.10	1.36	0.89
	Pipe	1.43	1.03	0.97
Underwater	Sheet pile	0.94	0.78	0.71
	Pipe	0.96	0.72	0.81

2 for transverse weld specimens and 4 for longitudinal weld specimens. By adopting n , the formula implicitly assumes that the total load is shared equally by welds in the same cross section of specimen in spite of slight asymmetry in the weld shape. Weld ductility, a normalized deformation factor, is defined as:

$$\gamma = \frac{\Delta_{\max}}{s} \quad (2)$$

where, γ is the ductility factor, Δ_{\max} is the measured weld deformation of the first fractured weld at its maximum applied

load, and s is the weld size of the first fractured weld. The definition of the weld size (JIS Z3001) is illustrated in Fig.4. After tests, failure modes are examined.

3. EXPERIMENTAL RESULTS AND DISCUSSIONS

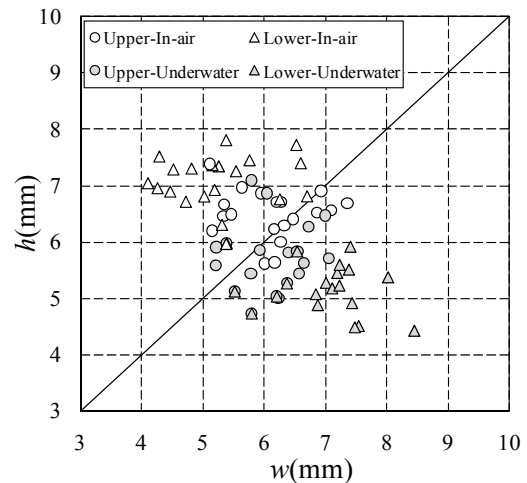
3.1 Inspections on Fillet Welds

Profile features of fillet welds are examined through statistical data measured by laser displacement sensor. Weld defects, such as pits and blow holes are inspected through the dye penetration test (JIS Z2343) and the radiographic examination (JIS Z3104). The radiographic examination is only performed on STK400 specimens. After weld strength tests, visual inspection is also conducted to examine weld undercut and weld penetration at weld roots.

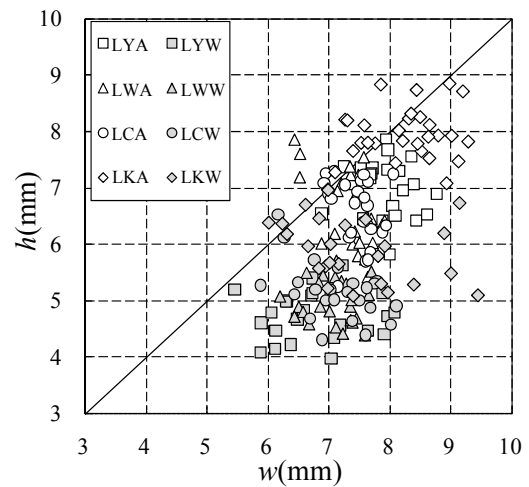
(1) Weld profile features

One obvious finding is that profiles of underwater welds are more irregular and deviated from the idealized shape of an isosceles triangle when compared with those of in-air welds as shown in Fig.5. Moreover, although the weld leg length is specified as 6 mm for both leg lengths h and w (see Fig.4 for the definition), weld profiles exhibit distinct trends related to welding environments and welding positions. Fig.6 shows h and w of all the weld beads, Table 5 summarizes an average h/w value of each weld assembly type.

Generally, underwater welds show h smaller than w in both weld orientations, with all h/w values being smaller than 1. Note that there are an upper side and a lower side of the cover plate in a transverse weld specimen, as previously shown in Fig.3. In underwater cases, transverse welds on the upper side exhibit h/w values close to 1, with 0.94 for the sheet pile case and



(a) Transverse weld

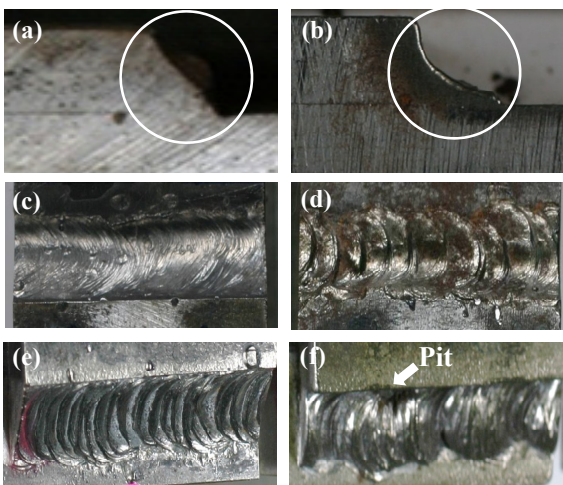


(b) Longitudinal weld

Fig.6 Weld leg length

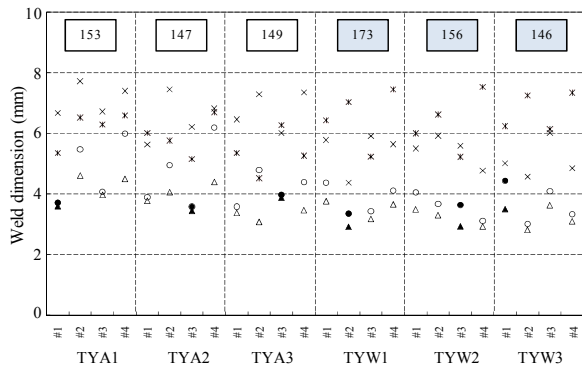
0.96 for the pipe case, while transverse welds on the lower side and longitudinal welds exhibit h/w values ranging from 0.72 to 0.81. This can be explained by welding positions and electrode angles in welding process, the better welding visibility and operability in the upper sides of transverse welds would help welders to produce welds closer to what is specified.

In sheet pile specimens, transverse in-air welds on the upper side with bead numbers #1 and #3 exhibit concave profiles comparing with the ones on the lower side with bead numbers #2 and #4 which exhibit convex profiles. Weld dimensions of the sheet pile specimens are shown in Fig.7 along with the first fractured weld and maximum load obtained in the weld strength tests. It is observed that although not always failing at the smallest weld, transverse welds made in air are found to be unlikely to fail on the lower side, where actual weld throat a' as defined in Fig.4 is considerably larger than weld throat a defined in JIS Z3001 as shown in Fig.7(b) and (d). However, no similar observation is found in

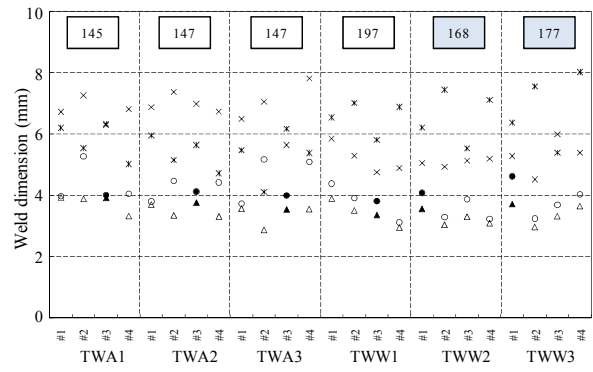


(a)TKA (b)TKW (c)TYA (d)TYW (e)LYA (f)LYW

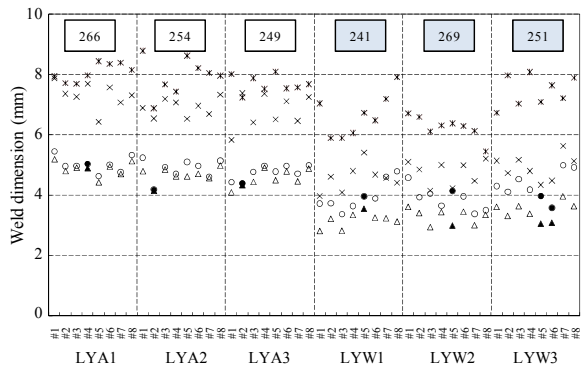
Fig.5 Weld profiles



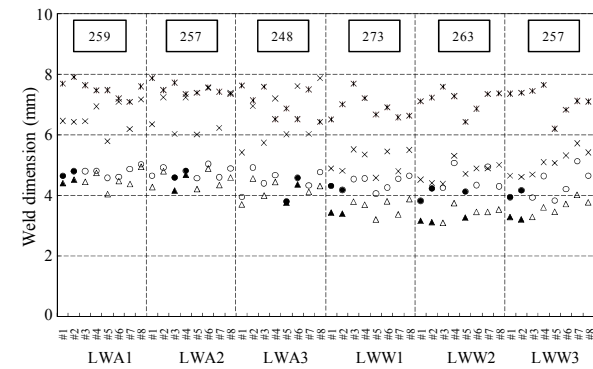
(a) Longitudinal welds on SY295 steel plate



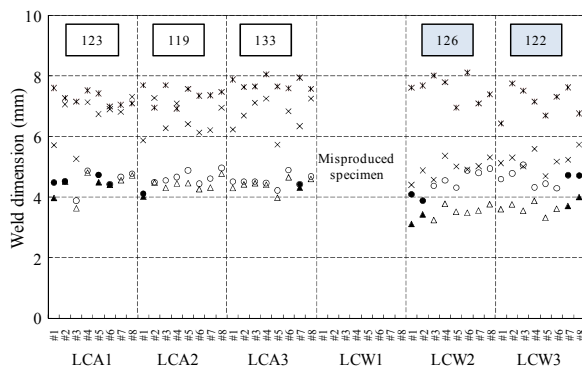
(b) Transverse welds on SY295 steel plate



(c) Longitudinal welds on SYW295 steel plate



(d) Transverse welds on SYW295 steel plate



(e) Longitudinal welds on corroded SY295 steel plate

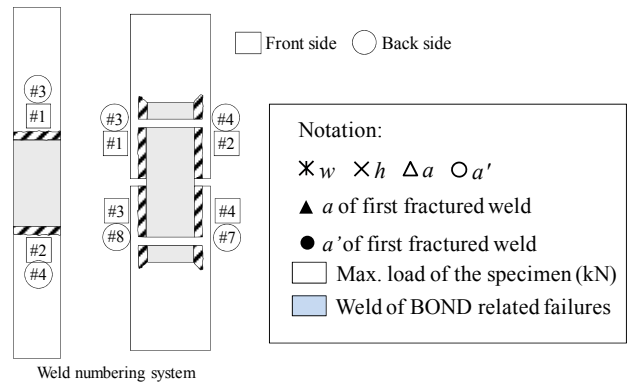


Fig.7 Weld dimensions and first fractured welds for steel sheet pile specimens

transverse underwater welds which do not show a typical failure mode at weld deposit (DEPO) in the strength tests as will be discussed in 3.4.

As for different base steel materials and structural types, there is no obvious correlation found either between weld profiles and base steels or between weld profiles and structural types. Curvature of the pipe ($\phi 216.3$ mm) used in this study does not seem to affect weld profiles significantly.

(2) Weld defects

Eleven surface-breaking defects, including circular ones with a diameter 1 to 3 mm and line-shaped ones with a length around 2 mm, are found in eight

specimens out of twenty-two underwater weld specimens. There is no defect found in in-air welds. It is shown that more defects are found in longitudinal welds in terms of weld orientation in this study. Two blow holes are found in LKW2#2 and TKW2#4 with diameters of 1.2 and 2.0 mm, respectively, by the radiographic examination.

After the strength tests, specimens are cut, and weld cross sections are inspected visually. Regardless of welding environments, slight weld undercut is found at base plates of transverse welds on the upper side and at cover plates of transverse welds on the lower side, while no noticeable weld undercut is found in longitudinal welds. It is also observed that most underwater welds,

regardless of weld orientations, bear incomplete weld penetration at roots to a slight extent.

Weld defects are expected to reduce weld strength. Some welds with defects fail in the strength tests, but others do not. In the similar manner, welds with defects do not show any obvious correlations with weld failure mode, strength, or ductility factor in this study. Plausible causes may include that the weld defects are just too small and few to present significant effects and that some other aspects, such as weld size and weld material properties, dominate the mechanical properties of fillet welds.

3.2 Load-Deformation Responses

Load-deformation curves of the first fractured weld in the weld assembly, one of each assembly type, are plotted in Fig.8. Generally, welds in the same assembly type exhibit similar load-deformation responses for most assembly types. The load in this figure is the total load in the specimen, and the deformation is the displacement measured at the end of the first fractured weld by a clip gauge.

Most of underwater welds show a larger ultimate load than that of their counterpart in-air welds. However, due to the significantly smaller weld throat, LKW with an average weld throat of 3.7 mm has a smaller ultimate load than LKA with an average weld throat of 5.0 mm.

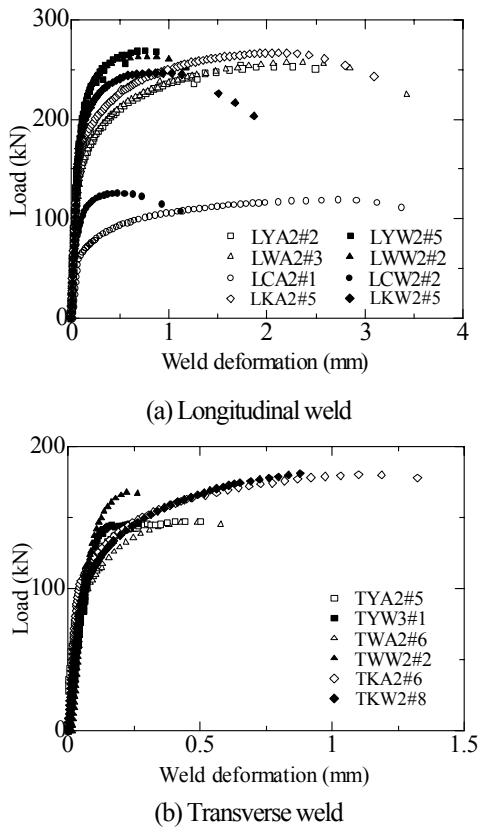
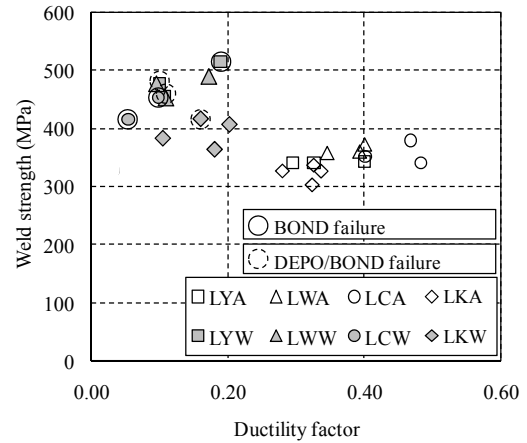
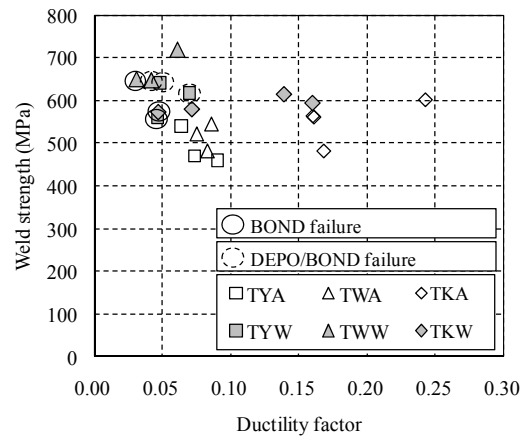


Fig.8 Load-deformation curves



(a) Longitudinal weld



(b) Transverse weld

Fig.9 Weld strength versus ductility factor

It is also observed that all underwater weld specimens show significantly smaller fracture deformation than their counterpart in-air welds. In the load-deformation curves, there is always “plateau” before in-air welds fail, while for underwater welds, fracture comes soon after their maximum loads.

3.3 Weld Strength and Ductility

Weld strengths and ductility factors previously defined in 2.1 are plotted for all specimens in Fig.9. For the sake of comparison between in-air and underwater welds, strength increase and ductility decrease of underwater welds are calculated in percent when compared with their counterpart in-air welds as shown in Fig.10. Underwater welds show a strength increase ranging from 6.9% to 41%, while ductility decrease is about 50% for most weld assemblies. The weld strength and ductility are examined in terms of base steel materials, weld orientations, and corrosion of base steel in the following.

(1) Material types of base plates

Whether base plates are flat sheet pile or curved pipe,

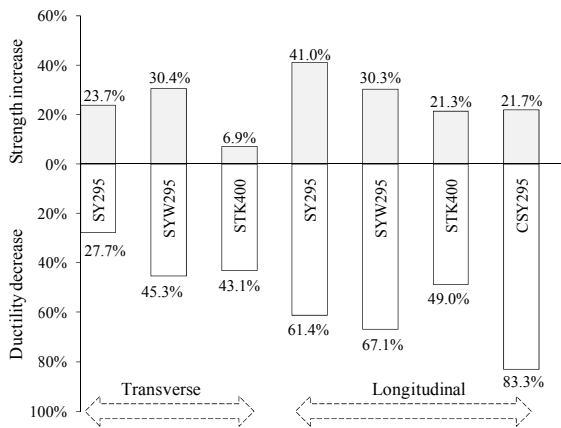


Fig.10 Relative changes of strength and ductility from in-air welds to underwater welds

the shape difference of base plates is not found to be influential to either weld strength or ductility. On the other hand, differences in chemical compositions do affect strength and ductility significantly. As listed in Table 3, for sheet piles, SY295, SYW295, and CSY295, the carbon equivalent ranges from 0.379 to 0.433, which is much higher than 0.230 of the pipe material, STK400. Strength increase of underwater welds on sheet pile materials is 30% on the average, which is about twice as large as 14% of the pipe material, while ductility decreases for different materials are nearly the same at around 50% except transverse welds on SY295 and welds on CSY295. Welds on CSY295, which exhibit a strength increase of 22% but a drastic ductility decrease of 83%, are not discussed here but will be discussed in detail in the following section (3).

(2) Weld orientations

Mechanical properties of welds on different base steels are affected by weld orientations to a different degree as observed in Fig.10. As for welds on SY295, when the weld orientation is changed from transverse to longitudinal, strength increase and ductility decrease are nearly doubled from 24% to 41% and from 28% to 61%, respectively. Welds on STK400 show a greater change in strength but smaller in ductility, with strength increase tripled from 6.9% to 21% and ductility decrease remained at around 50%. However, welds on SYW295 are not affected by weld orientations and strength increase is about 30% for both directions.

Moreover, longitudinal fillet welds exhibit more sensitivity to wet welding environment, with a strength increase of 29% and a ductility decrease of 65% on average, than transverse fillet welds with a strength increase of 20% and a ductility decrease of 49%. It should be noted that the strength of welds produced in air, which fail at weld deposit (DEPO), tends to increase with ductility factor as shown in Fig.9(a) and (b). This

shows that weld strength is affected by how much weld beads can deform before they reach their maximum loads. For longitudinal welds, it is well known that shear stress is non-uniform along the weld beads and the shear stress is larger at two ends and smallest at the center¹³). The small weld ductility will prevent additional load from being shared by weld in the central region because the two ends of the weld bead fracture soon after they yield. Consequently, the smaller the deformation capacity at weld ends in a longitudinal weld, the smaller weld strength will be. The same explanation is not applicable to the welds produced underwater because they do not show a typical DEPO failure as will be discussed in 3.4.

(3) Corrosion effects

It can be observed from Fig.10 that underwater welds on corroded SY295 steel exhibit a strength increase of 22%, but a drastic ductility decrease of 83% when compared with their counterpart in-air welds. As for absolute values indicated in Fig.9(a), the LCA welds have the largest ductility factor with an average value of 0.45, but their counterpart LCW welds have the smallest ductility factor with an average value of 0.08 among all longitudinal welds.

To examine the corrosion effects on strength and ductility of fillet welds, CSY295 and SY295 are compared. Although the chemical compositions of CSY295 and SY295 are quite similar as shown in Table 3, LCW welds with an average strength of 435 MPa exhibit a smaller strength by 11% than LYW welds with an average strength of 482 MPa. However, for corresponding in-air welds, LCA welds have slightly larger strength with an average strength of 357 MPa than LYA welds with an average strength of 342 MPa. This phenomenon can be explained by ductility of those welds. LCW welds show a ductility factor of 0.08, while LYW welds show 0.13, which is 1.6 times larger than LCW. As for LCA and LYA welds, the ductility factors are 0.45 and 0.34, respectively. The smaller ductility of LYA results in the smaller strength than LCA welds. The ductility factor of LCW is turned out to be the smallest among all longitudinal welds, which will be examined in the following sections of failure modes and hardness distribution.

One observation from the visual inspection after the strength tests is that LCW3#3 shows incomplete weld fusion due to corrosion pits in the base plate, which may have contributed to its failure mode. Besides the incomplete fusion, there is no obvious correlation found between corrosion effects, thickness reduction and surface roughness of base plates, and weld properties in terms of weld strength and ductility in this study.

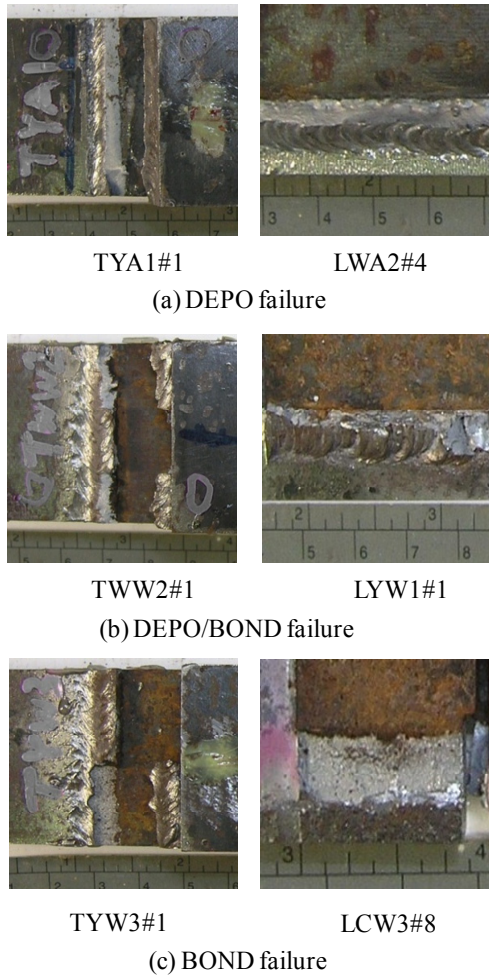


Fig.11 Comparison of failure modes

Considering only five specimens with corroded base plates are used in this study, more study may be needed to draw a further conclusion.

3.4 Failure Modes

In Fig.9, failure modes are also indicated. It is observed that all in-air welds exhibit ductile fracture at DEPO, but underwater welds indicated with circles in Fig.9 fail either at the boundary (BOND) between DEPO and base metal or with a combination of DEPO and BOND. Different failure modes of fillet weld joints are representatively shown in Fig.11. All six underwater specimens with SY295 as the base steel, TYW and LYW, fail at BOND or DEPO/BOND regardless of the weld orientations. All two underwater specimens of CSY295, LCW, exhibit brittle fractures at BOND with little deformation observed in weld metals as shown in Fig.11(c), resulting in low ductility of LCW welds.

With base steels of STK400 and SYW295, two out of eight specimens of TKW and LKW and two out of six specimens of TWW and LYW fail at BOND or DEPO/BOND. As shown in Table 3, considering the differences in carbon equivalent, the findings in failure

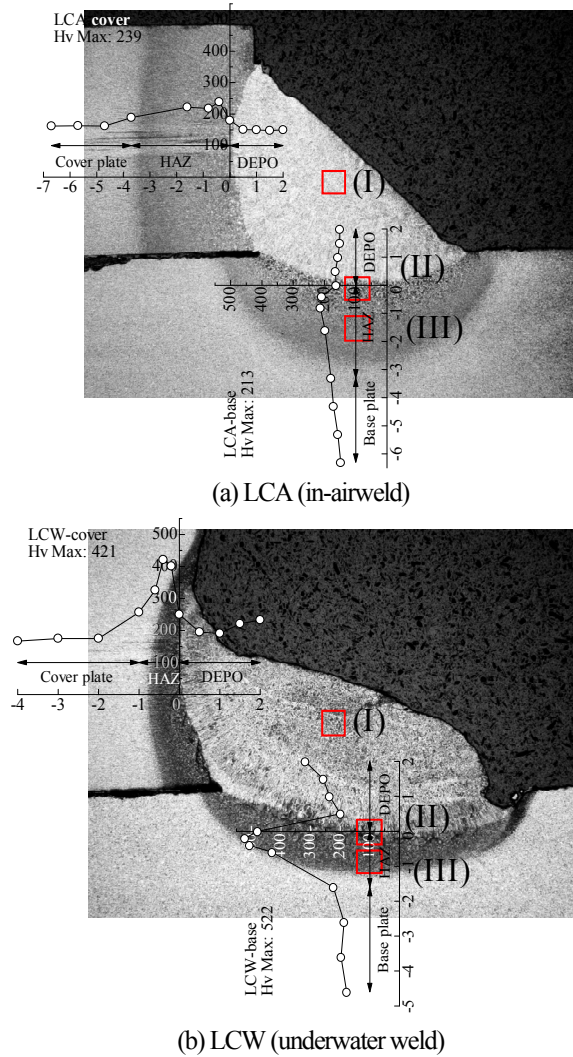


Fig.12 Hardness distribution in welds

modes suggest that “milder” steels STK400 and SYW295 with lower carbon equivalents of 0.230 and 0.379, respectively, have better weldability in underwater environments than “tougher” steels SY295 and CSY295 with higher carbon equivalents of 0.430 and 0.433, respectively, although all the base steels do not show any problem in open air welding.

3.5 Weld Hardness and Microstructures

Welding is a thermo-mechanical process, and weld properties are closely related to thermal conditions which affect weld microstructures and in turn mechanical properties. This section discusses results from Vickers hardness tests (JIS Z2244) and metallographic examinations of fillet welds. The specimens for hardness tests are produced simultaneously with specimens for the strength tests to ensure the same welding conditions.

(1) Hardness distribution

Fig.12 shows photos of polished and etched cross

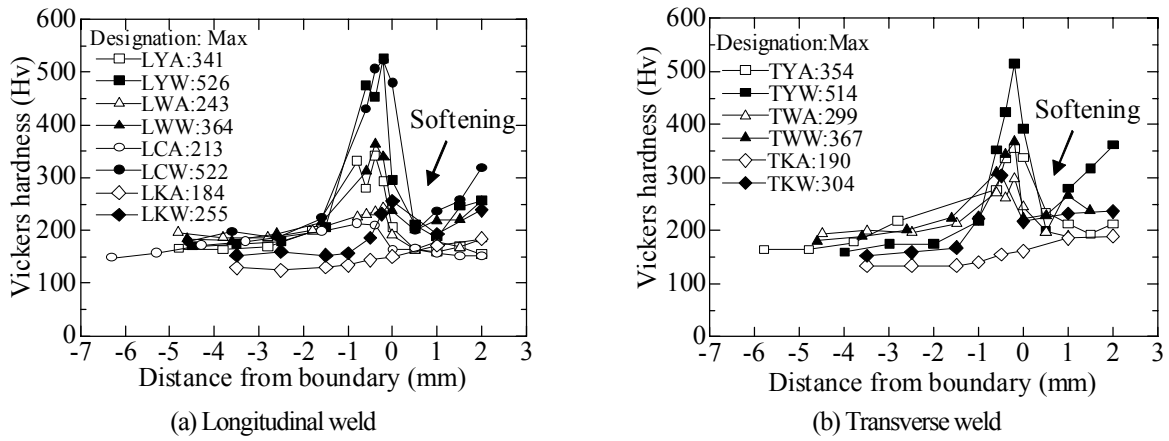


Fig.13 Hardness distribution on the base plate side

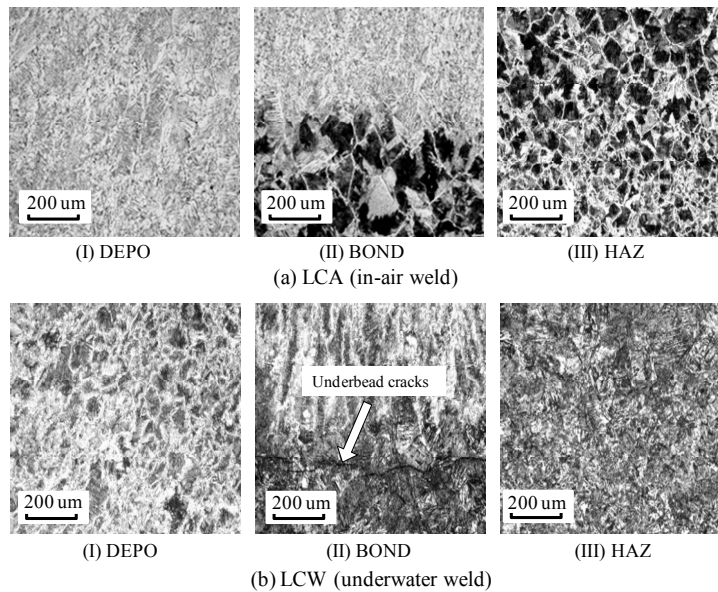


Fig.14 Weld microstructures

sections of LCA and LCW welds with Vickers hardness results superimposed. Points for data acquisition are located along the arrows in the figure. The hardness results on the side of base plate are summarized in Fig.13. Three windows in each photo of Fig.12 signify the areas where microstructure images, shown in Fig.14, are taken. These photos are representative to reveal general features of fillet welds examined in this study.

As shown in Fig.12, hardness peaks can be found in the coarse grained region of HAZ in both in-air and underwater welds except LKA and TKA of STK400. By referring to Table 3, the positive correlations between hardness peak values and carbon equivalents of base steels are found to be more pronounced in underwater welds. Underwater welds on SY295 that has the largest carbon equivalent of the three base steels show the highest hardness, 526 Hv for LYW, 522 Hv for LCW, and 514 Hv for TYW, while underwater welds on STK400 that has the lowest carbon equivalent, show only 255 Hv for LKW and 304 Hv for TKW.

Moreover, underwater welds are observed with hardness softening in the boundary regions between DEPO and HAZ as indicated in Fig.13. Also, due to the rapid quenching in the wet environment, heat transfer is limited in a smaller region, resulting in a smaller HAZ size of 1 to 2 mm and higher HAZ hardness of 310 to 526 Hv for underwater welds, whereas they are 3 to 4 mm and 198 to 375 Hv, respectively for in-air welds. In addition, as indicated in Fig.14(b)(II), there are underbead cracks found in the boundary areas between DEPO and HAZ in underwater welds of TYW, LYW, and LCW welds, which are on SY295 and CSY295 steels. It should be noted that there are more underbead cracks in LCW welds than the other two. Whereas no crack is observed in underwater welds of TWW, LWW, TKW, and LKW welds, which are on SYW295 and STK400.

It is known that the thickness of base plate affects cooling rate and weld hardness since the base plate acts as a heat sink^{14,15}. This can be observed in LYA and

LCA. LCA welds on CSY295 with the base plate thickness varying from 6 to 8 mm have the maximum hardness of 213 Hv in HAZ, while LYA welds on SY295 with the larger base plate thickness of 12.7 mm have the maximum hardness of 341 Hv in HAZ. However, for underwater welds the thickness of base plate has little influence on the peak hardness. As shown in Fig.13(a), the hardness distributions of LCW and LYW are quite similar, and the maximum values are 522 Hv and 526 Hv, respectively. One explanation for this hardness insensitivity to the base plate thickness in the underwater welding is that the base plate, which plays an important role as a self-quenching source in open air welding, is greatly substituted by ambient water; therefore, the effect of the base plate thickness is not obvious in the underwater welding.

(2) Weld microstructures

There are similar tendencies of microstructure distributions within welds made in the same environment despite of differences in base steels. As representatives, microstructures of LCA and LCW welds are shown in Fig.14. The microstructures of DEPO are shown in Fig.14(a)(I) and 13(b)(I). DEPO in LCA is mainly composed of ferrite and pearlite with 150 Hv, and DEPO in LCW is also composed of ferrite and pearlite with hardness ranging from 180 to 300 Hv, where hardness is lower near the boundaries between DEPO and HAZ, and higher at the center of weld metal as previously shown in Fig.13(a). HAZ in LCA, as shown in Fig.14(a)(III), is composed of ferrite and perlite with 200 Hv, while HAZ in LCW, as shown in Fig.14(b)(III), is dominated by martensite with 500 Hv. This distinct mechanical mismatching over base steel CSY295 with 150 Hv is reported to have detrimental effects to weld joints with presence of cracks in BOND regions and HAZ¹⁶⁾. In addition, underwater welds on thinner base steels are observed to have more underbead cracks. Based on the findings in hardness distributions and weld microstructures, low ductility of LCW welds would be caused by underbead cracks and hardness mismatching in BOND regions.

4. FINITE ELEMENT MODELING

The main objective of the finite element (FE) analysis presented in this section is to develop finite element modeling procedures for underwater welds, which can reproduce the experimental results and predict mechanical behavior of underwater welds that are not examined in the experimental study.

Without introducing significant errors, HAZ is usually neglected in FE models for in-air welds.

However, it is the critical part to distinguish mechanical properties of underwater welds from those of in-air welds, and modeling HAZ of underwater welds is indispensable to predict their mechanical behaviors accurately. For FE analysis, mechanical properties of HAZ need to be prepared in the form of stress-strain relationships as input data. In this study, the yield stress and tensile strength are estimated from Vickers hardness values by using empirical relationships. In the following, the constitutive relationships of HAZ and DEPO are derived from Vickers hardness values, and then geometric features of underwater weld details are modeled. By using the developed model, FE analysis is performed by using the general purpose FE software, ABAQUS¹⁷⁾, to reproduce the experimental results.

4.1 Constitutive Relations of HAZ and DEPO

This paper assumes stress-strain relationships of HAZ and DEPO follow the power law as:

$$\sigma_t = A\varepsilon_t^n \quad (3)$$

where, σ_t is true stress, ε_t is true strain, n is hardening exponent, and A is hardening coefficient. To determine the power law in Eq. (3), three parameters are required: hardening exponent n , hardening coefficient A , which define the shape of the constitutive curves, and true fracture strain ε_t^f or true fracture stress σ_t^f , either of which defines the fracture point of the material. Based on empirical equations proposed by Akselsen et al.¹⁸⁾, the hardening exponent n can be determined from the cooling time of steel from 800°C to 500°C, $t_{8/5}$, as:

$$n = 0.065(t_{8/5})^{0.17} \quad (4)$$

where, $t_{8/5}$ is a function of Vickers hardness and chemical compositions of the metal, the derivation of $t_{8/5}$ from Vickers hardness and chemical compositions can be found in detail in Watanabe et al.¹²⁾. Hardening coefficient A , according to Eq. (3), can be derived as:

$$A = E^n / (\sigma_t^y)^{n-1} \quad (5)$$

where, E is Young's modulus of steel, 205 GPa in the present study, and σ_t^y is true yielding stress, which can be estimated by the empirical equation from Akselsen et al.¹⁸⁾ as:

$$\sigma_n^y = 3.1H_v(0.1)^n - 80 \quad (6)$$

where, σ_n^y is nominal yield stress in MPa, and H_v is Vickers hardness value.

The third parameter, ε_t^f , can be obtained from Eq. (7) which is derived from regression analysis based on the test data by Suzuki and Tamura¹⁹⁾. The regression

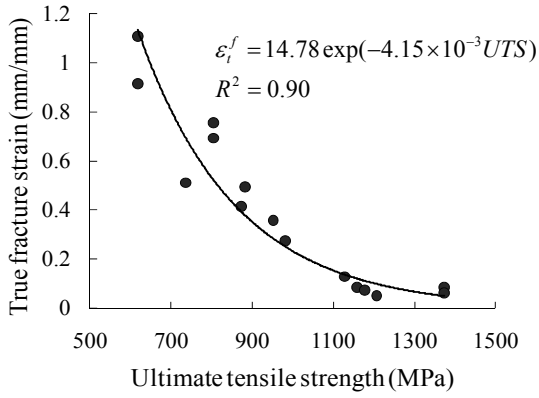


Fig.15 Proposed equation using test data by Suzuki and Tamura¹⁹⁾

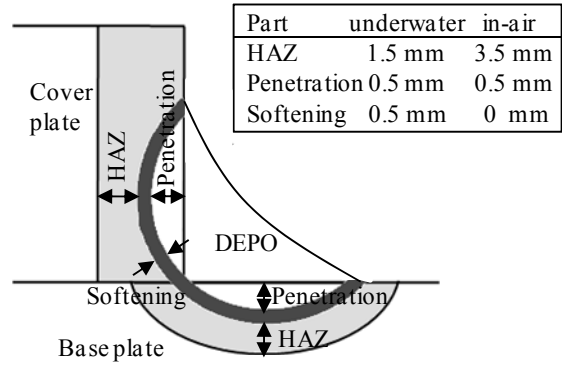
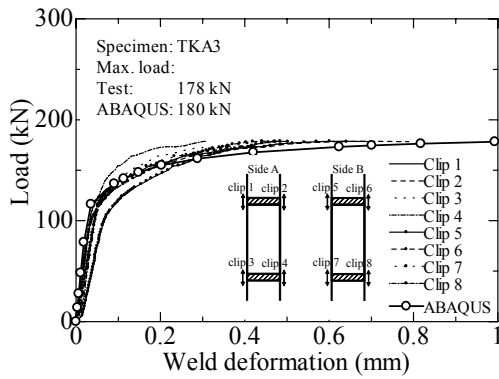
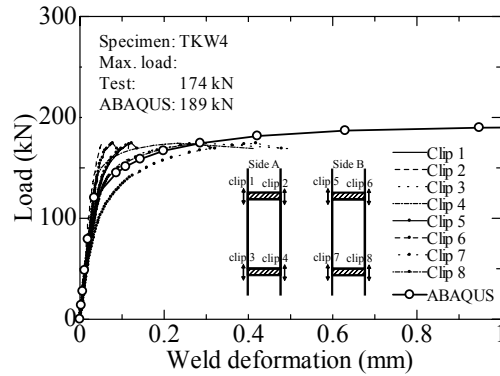


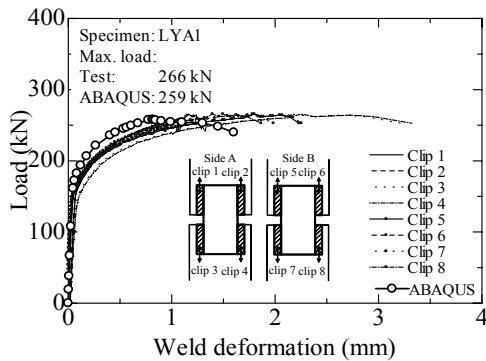
Fig.16 Geometrical model for welds



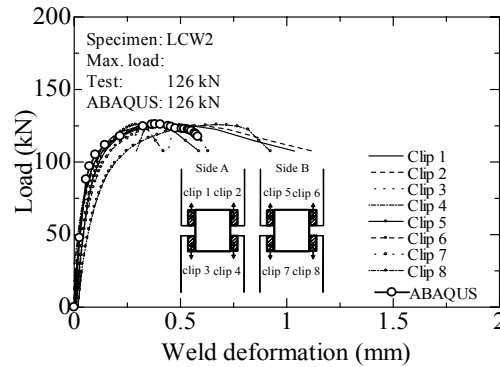
(a) Transverse in-air weld



(b) Transverse underwater weld



(c) Longitudinal in-air weld



(d) Longitudinal underwater weld

Fig.17 Comparison of load-deformation relationships between experiment and FEA

curve and the test data are plotted in Fig.15.

$$\varepsilon_f^f = 14.78 \exp(-4.15 \times 10^{-3} UTS) \quad (7)$$

where, UTS is ultimate tensile strength in MPa, and can be obtained using Eq. (8) for HAZ and Eq. (9) for DEPO, which are proposed by Akselsen et al. in Ref. 18) and Ref. 20), respectively.

$$UTS_{(HAZ)} = 3.5H_v(1-n)\left(\frac{12.5n}{1-n}\right)^n - 92 \quad (8)$$

$$UTS_{(DEPO)} = 3.5H_v(1-n)\left(\frac{12.5}{1-n}\right)^n - 50 \quad (9)$$

Given Vickers hardness values, the stress-strain relationship of

HAZ and DEPO can be determined for the weld of interest based on the above equations.

4.2 Geometric Models

Another difficulty in modeling is geometric complexity of welds. Modeling a precise weld bead is time consuming, hence, in this study, weld leg lengths, h and w , and weld throat, a , are used to define a weld cross section, which is uniform along the weld bead. Weld penetrations and the regions with hardness softening in underwater welds are simplified as shown in Fig.16. The size of each region is determined from pre-fracture macrostructural examination. The regions

of penetration and softening are assumed to have the same chemical compositions as the weld metal even though the fusions from parent steels could change the chemical compositions in these parts to a small extent²¹).

Strictly speaking, specimens are not symmetric in geometry about the center lines or the mid-plane of the base steel due to geometrical differences among welds. However, for computational efficiency, only 1/8 of each specimen is modeled by assuming the asymmetry is too small to affect the mechanical behavior of welds, and taking advantage of symmetries. Besides, the weld dimensions used in the FE analysis are the average values of all weld beads in the concerned specimen.

4.3 Finite Element Analysis Results

Load-weld deformation curves from analyzed results are plotted in Fig.17 with experimental results for TKA3, TKW4, LYA1, and LCW2. Generally, the FE model proposed in this study can predict the maximum load of a fillet weld specimen. In all examined cases, errors are found to be less than 10% of the test results.

Fracture deformation for longitudinal welds is predicted within 30% error, and that for transverse welds is considerably overestimated. This may be explained by a uniform stress distribution due to a uniform cross section along the transverse weld bead in the analyzed model. The uniform stress distribution causes every cross section along the bead to fracture simultaneously, resulting in larger weld deformation than that obtained in the experiment, where cross sections of a weld bead are not uniform along the weld bead and failure of weld may not occur simultaneously at every cross-section.

5. CONCLUSIONS

Fillet weld joints made by underwater wet welding were studied experimentally together with their counterpart weld joints made in open air with respect to weld strength, ductility, and failure modes in this study. Differences in mechanical properties of fillet welds between in-air and underwater welds were investigated through the strength tests of fourteen weld assembly types featuring two welding environments, two base steel structural types, four base steels, two weld orientations, and corrosion effect. The Vickers hardness tests and microstructure examinations were complemented for further insights into underwater weld joints. The modeling method in the FE analysis was proposed to reproduce experimental results. Main conclusions of this study are:

- (1) Underwater fillet weld joints have larger strength but smaller ductility than their counterpart in-air weld joints. Strength increases vary from 6.9% to 41% depending on weld assembly types, while ductility decrease is about 50% for the most weld assemblies.
- (2) When welds change from transverse orientation to longitudinal orientation, strength increases are nearly doubled from 23.7% to 41.0% on SY295 steels, tripled from 6.9% to 21.3% on STK400 steels and unchanged at around 30% on SYW295 steels.
- (3) Underwater welds on corroded SY295 steel show a drastic 83% decrease in ductility factor when compared with those on pristine SY295 steels. This is caused by underbead cracks coupled with hardness mismatching which incur brittle fractures in BOND of underwater weld joints on the thinner base plate.
- (4) Underwater welds have considerably larger hardness in HAZ than in-air welds, especially for sheet pile steels, and the peak hardness and carbon equivalent of base steels show a positive correlation. The thickness of base plate exhibits little influence on the hardness distribution of underwater welds, which is different from the in-air case.
- (5) Although all base steel materials used in this study do not exhibit any problem in in-air air welding, their underwater weldabilities depend on their carbon equivalents, and SY295 has the lowest underwater weldability among STK400, SYW295, and SY295.
- (6) By estimating material properties of welds from Vickers hardness and assuming a uniform cross-section along the weld bead with average dimensions, the maximum load of weld joints can be accurately predicted in the FE analysis for both in-air and underwater welds.

ACKNOWLEDGMENT:

This research was partially supported by The Japan Iron and Steel Federation and Nagoya University. The raw data of thicknesses and surface profiles of corroded sheet piles were provided by Professor Katashi Fujii of Hiroshima University. The authors would like to acknowledge their supports.

References

- 1) Liu, S., Maintenance and repair welding in the open sea, *Welding Journal*, 84(11), pp.54-59, 2005.
- 2) Wernicke, R. and Billingham, J., Underwater wet repair welding and strength testing on pipe-patch joints, *Journal of Offshore Mechanics and Arctic Engineering*, ASME, 120(4), pp.237-242, 1998.
- 3) Kinugawa, J., and Fukushima, S., Influence of equivalent carbon contents of steels on proportions of martensite, hardness and susceptibility to cold cracking at coarse-grained regions in underwater wet welding, *Welding*

- Society Journal*, 51(3), pp.45-51, 1982 (in Japanese).
- 4) Ibarra, S., Grubbs, C. E. and Olson, D. L., Metallurgical aspects of underwater welding, *Journal of Metals*, 40(12), pp.8-10, 1988.
 - 5) Pope, A., Teixeira, J., Dos Santos, V., Paes, M., and Liu, S., The effect of nickel on the mechanical properties of high-oxygen underwater wet welds, *Journal of Offshore Mechanics and Arctic Engineering, ASME*, 118(2), pp.165-168, 1996.
 - 6) West, T. C., Mitchell, G., and Lindberg, E., Wet welding electrode evaluation for ship repair, *Welding Journal*, 69(8), pp.46-56, 1990.
 - 7) Rowe, M. D., Liu, S., and Reynolds, T. J., The effect of ferro-alloy additions and depth on the quality of underwater wet welds, *Welding Journal*, 81(8), pp.156S-166S, 2002.
 - 8) Akselsen, O. M., Fostervoll, H., Harsvaer, A., and Aune, R., Weld metal mechanical properties in hyperbaric GTAW of X70 pipeline, *International Journal of Offshore and Polar Engineering*, 16(3), pp.233-240, 2006.
 - 9) Zhang, X. D., Chen, W. Z., Ashida, E., and Matsuda, F., Metallurgical and mechanical properties of underwater laser welds of stainless steel, *Journal of Material Science & Technology*, 19(5), pp.479-483, 2003.
 - 10) Coastal Development Institute of Technology, *Port Steel Structure Corrosion-Prevention and Repair Manual*, Coastal Development Institute of Technology, Japan, 1997 (in Japanese).
 - 11) Department of The Navy Naval Sea Systems Command, *U.S. Navy Underwater Cutting & Welding Manual NAVSEA S0300-BB-MAN-010*, Direction of Commander, Navy Naval Sea Systems Command, Washington, D.C., 2002.
 - 12) Watanabe, N., Kitane, Y., and Itoh, Y., Modeling of joint behavior of steel pipes repaired with steel plate by underwater wet welding, *Journal of Structural Engineering, JSCE*, 55A, pp.903-914, 2009 (in Japanese).
 - 13) Suzuki, H., *Recent Welding Engineering*, Corona Publishing Co., Ltd., Tokyo, Japan, 1982 (in Japanese).
 - 14) Yang, L. J., The effect of specimen thickness on the hardness of plasma surface hardened ASSAB 760 steel specimens, *Journal of Materials Processing Technology*, 185, pp.113-119, 2007.
 - 15) Shehata, F., Technical report: Effect of plate thickness on mechanical properties of arc welded joints, *Material & Design*, 15(2), pp.105-110, 1994.
 - 16) Zhang, Z. L., Thaulow, C., Hauge, M., Effects of crack size and weld metal mismatch on the HAZ cleavage toughness of wide plates, *Engineering Fracture Mechanics*, 57(6), pp.653-664, 1997.
 - 17) Dassault Systèmes Simulia Corp. *ABAQUS/Standard user's manual, version 6.8*, 2008.
 - 18) Akselsen, O.M., Rorvik, G., Onsoien, M.I., and Grong, Ø., Assessment and predictions of HAZ tensile properties of high-strength steels, *Welding Journal*, 68(9), pp.356-362, 1989.
 - 19) Suzuki, H. and Tamura, H., Weldability of high-strength steels evaluated by ductility test on synthetic heat-affected zone, *Iron and Steel*, 47(3), pp.482-484, 1961 (in Japanese).
 - 20) Akselsen, O. M. and Grong, Ø., Prediction of weld metal Charpy V notch toughness, *Materials Science and Engineering*, A159, pp.187-192, 1992.
 - 21) Mellor, B. G., Rainey, R. C. T., and Kirk, N. E., The static strength of end and T fillet weld connections, *Materials and Design*, 20, pp.193-205, 1999.

(Received September 24, 2009)